Results in Engineering 12 (2021) 100304

Contents lists available at ScienceDirect

Results in Engineering

journal homepage: www.sciencedirect.com/journal/results-in-engineering

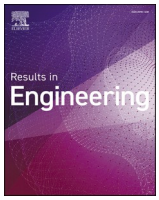

Evaporation characteristics during decompression of liquified CO_2 from a conical-shaped vessel

Osama M. Ibrahim *, Per Morten Hansen, Dag Bjerketvedt, Knut Vågsæther

The University of South-Eastern Norway, Faculty of Technology, Natural Sciences, and Maritime Sciences, Department of Process, Energy and Environmental Technology, Kjølnes Ring 56, 3918, Porsgrunn, Norway

ARTICLE INFO

Keywords:
CO_2 depressurization
Divergent cross-section
Evaporation wave
Isentropic expansion
Metastable state

ABSTRACT

Safe transport of pressurized CO_2 requires a profound knowledge of the processes' effect during the phase transition on catastrophic failure of a tanker filled with liquid CO_2. This study presents experimental results and analyses associated with the characteristics of expansion waves during depressurization of liquified CO_2 in a divergent cross-section vessel. It explores the rarefaction and evaporation waves velocities analyzed in different three vessel's regions based on the pressure records. Results showed that the evaporation wave velocity increased downward with decreasing cross-section and increased liquid volume fraction. Also, the upstream state properties after the isentropic expansion in the metastable region were determined. The results were compared with previously achieved outcomes of CO_2 decompression from a constant cross-section rectangular duct.

Comparisons indicated significant differences in the wave pattern. So, expansion waves velocities varying in different vessel regions while they were nearly constant for the duct. The evaporation wave velocities were nearly identical for the duct and the upper conical vessel's regions. But their divergence increased as the evaporation wave propagated downwards. Furthermore, the downstream two-phase flow in the conical vessel propagated in an increased cross-section toward the exit. In comparison, there was non-spontaneous two-phase propagation behind the evaporation wave due to the small exit cross-section in the rectangular duct. Additionally, during the isentropic expansion, the degree of superheat was higher for the conical vessel than the duct, resulting in significant discrepancies in the upstream flow properties.

1. Introduction

Climate change and global warming are now affecting almost every part of the world due to the augmented greenhouse consequences. The CO_2 emissions from human activities are the primary cause, whereby the burning of fossil fuels like gas, oil and coal are significant contributors. To achieve the Paris climate agreement goal of keeping the rising temperature below 1.5 °C, around 94 Gt CO_2 is projected to be captured and stored by 2050 [1]. Carbon capture and storage (CCS) systems have become a pivotal solution to create carbon-neutral sound technologies. There are other supplemented techniques utilized to ease CO_2 reduction and capturing. These include gasification, conventional combustion, fuel cells, and fuel efficiency enhancement. For instance, upgrading lignite by flotation enhances its heat content and reduces CO_2 releases during combustion [2,3].

Transport of a large amount of captured CO_2, as a part of carbon capture and storage systems (CCS), necessitates a deep understanding of associated hazards. Serious safety concerns emerge from an unexpected failure of a tank carrying pressurized-liquified CO_2 caused by external fire overheating, mechanical failure, or corrosion. The rapid release of CO_2 from such a container could lead to an explosive boiling and vaporization and may be described as a boiling liquid expanding vapour explosion (BLEVE). The suddenly freed energy from depressurization initiates strong pressure waves. That potentially promote devastating effects caused by missiles from container fragmentation. Additionally, a considerable amount of CO_2 discharges to the surroundings.

BLEVEs tend to occur as an outsized volume of liquid and vapour expanded in a short time (milliseconds). Consequently, the container walls cannot withstand the grown stress resulting in an explosion [4,5]. Initially, the pressurized liquified CO_2 is at equilibrium with the vapour phase above it and has a temperature higher than its atmospheric boiling point. Its temperature can far surpass its boiling point at a specified

* Corresponding author.
E-mail addresses: osama.k.ibrahim@usn.no (O.M. Ibrahim), per.m.hansen@usn.no (P.M. Hansen), dag.bjerketvedt@usn.no (D. Bjerketvedt), knut.vagsather@usn.no (K. Vågsæther).

https://doi.org/10.1016/j.rineng.2021.100304
Received 20 July 2021; Received in revised form 8 September 2021; Accepted 17 October 2021
Available online 11 November 2021

pressure. When the pressure drops rapidly, the liquid's state changes to superheated. The superheated liquid temperature would lay at any point in the metastable liquid region between the saturation and spinodal curves. However, the condition $(\partial P/\partial V)_T = 0$ is satisfied along the spinodal lines. This line signifies a limit temperature for the thermodynamic degree of superheating (SLT), and the liquid is unstable beyond it. The degree of superheat depends upon the depressurization rate, which, in turn, influences the bubbles' forming and developing mechanisms [6]. In general, at a low/medium degree of superheat, heterogeneous nucleation starts at the wall's surface or on particle impurities. The bubbles develop gradually in size resulting in a violent boiling process. During rapid depressurization and smooth wall's surface, homogeneous nucleation could occur in the liquid bulk. Moreover, the degree of superheat is high, which causes an intense spurt of multiple-phase flow [7].

Several models have suggested that explosion occurs when the liquid that entering the saturation dome becomes superheated. The earliest attempts made by Reid [7] to set the conditions under which BLEVE could arise mentioned that the liquid's temperature should reach the superheat limit temperature (SLT). Thus, the temperature should approach the spinodal curve, and the vapour's expansion occurs promptly due to the evaporation throughout the whole liquid [8]. Additionally, depressurization must be very rapid so that there is not enough time for heterogeneous nucleation to start on the container's walls. Conversely, other experimental studies denoted that it is not strictly necessary for BLEVE incidence to occur that the liquid temperature surpasses the SLT [9,10]. Explosive vaporization of CO_2 could also occur before it reaches SLT as CO_2 changes to the solid phase at atmospheric pressure by originating nuclei which promote liquid flashing [6]. Abbasi and Abbasi [11] reported results from previous experiments where SLT for CO_2 at 2.9 MPa was −6 °C.

When a rapid decompression of pressurized liquified CO_2 occurs inside a vertical vessel with smooth walls, the superheated liquid in the metastable region attains a high degree of superheating. The homogeneous nucleation proceeds in the liquid bulk during the evaporation process, and the liquid suddenly liberates its stored internal energy. The evaporation process initiates in a part of the liquid, and heat amount is extracted from it. So, the liquid's temperature and vapour pressure drop. The liquid temperature keeps dropping until it reaches boiling temperature. Simultaneously, the vapour pressure reduces towards atmospheric pressure. The rapid phase change with expanded vapour's volume results in multiple-phase bursting out of the vessel, and subsequently, generates a shock wave due to compression of the surrounding air [7]. This wave propagates upwards to the surrounding area with supersonic speed, followed by a primarily created vapour-liquid contact surface. As a subsequent response to the pressure drop, a rarefaction wave propagates with sonic speed downwards inside the vessel, followed by an evaporation wave. The evaporation wave could exemplify a limited zone where the phase transitions occur and travelling with almost constant velocity [12]. The propagation of the evaporation wave into a metastable liquid depends on superheat degree, and it is potentially promoted when the temperature approaches the superheat limit. When the superheat degree is low, the subsequent evaporation rate is insufficient to generate a severe explosion [13]. Noticeable studies on evaporation waves features have been done by Hill [14] and later Reinke et al. [15]. They characterized the bubble formation and movement of the propagated boiling front (photographically). Besides, they measured the velocities ahead of and behind the evaporation wavefront.

The difficulties of full-scale experiments involving phase transition and explosion to provide typical results necessitate numerical models computation. Published literature describes several models to estimate the two-phase flow properties behind the evaporation or condensation waves and the multi-phase flow behind the shock waves. The issued studies described either the two-phase flow dynamics or the shock wave and thermodynamic properties [16–19].

A model describing the phase transition process identifies flow thermodynamic properties by including an equation of state (EOS). Its function is to determine the state properties and the relation between them in the metastable region. Most EOS calculations are restricted to the equilibrium regions and need to extrapolate from the saturation properties to compute metastable state variables. Various EOSs have been used in depressurization and phase change models for different substances. However, Span-Wagner EOS (SW-EOS) [20] claimed to be the most accurate equation for CO_2 phase transition models. It is used in several types of research, for instance, by Giljarhus et al. [21] and Hansen [22]. SW-EOS has many solution versions, and this work uses the version presented by Mjaavatten [23]. SW-EOS is explicit in the Helmholtz free energy, whereby the thermodynamic properties are calculated as a function of temperature and molar volume.

Although some publications describe experimental work on CO_2 depressurization, very few of them have utilized a double-diaphragm rupturing mechanism with high-pressure or divergent cross-section vessels. Therefore, this study's originality provides new data and analysis of the evaporation characteristics during CO_2 decompression from a double-diaphragm conical rig compared with constant area containers. It focuses on two features: First, the rarefaction and evaporation waves' velocities, and waves propagation interaction during the phase transition. Second, the influence of the divergent cross-section on evaporation wave characteristics by drawing a comparison with previous results from constant cross-section tests.

2. Description of experimental arrangements and procedure

Small-scale experiments were carried out on a vertical double-diaphragm conical rig. This installation shows similarities with a shock tube. The main conical rig assembly is stainless steel (AISI 316) and comprises three parts, a conical vessel and two slip-on flanges. The conical vessel functions as a high-pressure section (HPS), while the middle flange operated as a medium-pressure section (MPS). The additional upper flange opens to an atmospheric chamber. It also holds the diaphragm that separates the MPS and atmospheric conditions under load. The conical vessel was securely fixed on the t-slot framing aluminium construction and tightly fastened with the flanges and diaphragms by eight bolts. The conical vessel has a volume of $480{\cdot}10^3$ mm^3 and an inside height of 383 mm. It has solid steel walls with an inclination of 4°, a thickness of 18,67 mm, and an inner surface roughness average of 3.2. The vessel has a bottom diameter of 9.37 mm and is strengthened with a cubic base to hold possible excess strain due to expansion waves propagating through the liquid to the bottom. It has two openings for inflow on the bottom and outflow on the top. Twelve holes for sensors are drilled on the vessel's sidewalls. There are six holes for pressure sensors on one side and six for temperature sensors on the opposite side.

The medium-pressure slip-on flange has a cylindrical middle-section with a diameter of 90.3 mm, a height of 80 mm, and a volume of $510{\cdot}10^3$ mm^3. Also, It has ½ " inlet/outlet opening fitted with a flexible metallic hose and connected to a three-way valve. Its function is to fill or evacuate the vapour CO_2 in/from the medium-pressure section (MPS). Besides, the slip-on flange is sealed with O-rings on both sides to ensure firmly pressing of the diaphragms, and in turn, to avoid any potential leaks. Fig. 1 illustrates schematic drawing (a) with a close-up of the conical vessel and an image (b) of the experimental set-up.

There are two aluminium diaphragm sets tightly fixed between flanges. One set between the high-pressure conical vessel (HPS) and MPS. Another diaphragm is set between the MPS and the atmospheric flange. The diaphragms are cut from Alfer aluminium blank sheets with three different thicknesses 0.3, 0.5, and 0.8 mm. Based on the results from a series of implemented tests, the diaphragms' combination was designated to be 1.4–1.5 mm for medium-pressure diaphragm (MP) and 1.5–1.6 mm for high-pressure one (HP). Gaskets made mainly of glass, aramid fibres, and nitrile binder were added to the diaphragms' two sides to seal the MPS properly. They were compactly pressed between

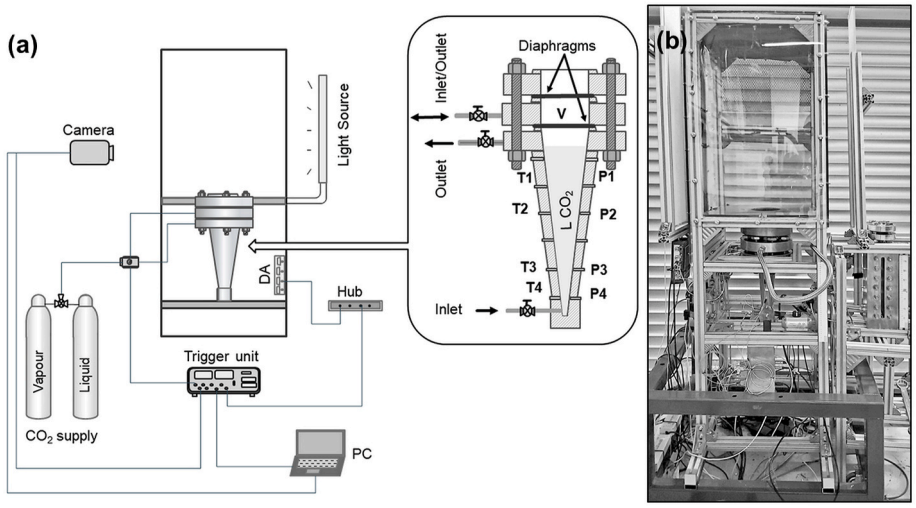

Fig. 1. (a) Set-up schematic drawing including an enlarged segment of the conical vessel details. (b) Installation image showing the conical rig and an auxiliary equipment.

the flanges.

The conical vessel (HPS) and medium-pressure flange (MPS) were separately filled from two industrial graded gaseous and liquid CO_2 cylinders until the pressure reached 5.2–5.6 and 2.6–2.8 MPa, respectively. Because the conical vessel's walls were untransparent, an additional rectangular duct with a glass window was used as a level gauge. The conical vessel and the rectangular duct connected through a control valve, and they were filled simultaneously to determine the liquid level. The MP diaphragm ruptured following an increase in the MPS pressure by opening the three-way valve. It was triggered through its connection with Quantum pulse generator composers 9500. Subsequently, the MPS pressure swiftly fell to the atmospheric, and the HP diaphragm ruptured due to the growth of pressure difference. The pressure inside the HP vessel was recorded using four Kulite XTM-190-2000G transducers attached on one side of the vessel wall. For temperature recording, three K-type thermocouples were fixed on the opposite sidewall. The same type of transducer is mounted on the MPS′ cylindrical section to record the MPS pressure. Likewise, a Kulite XTM-190-100G measured the overpressure generated after diaphragms' rupturing in the atmospheric chamber covered from all sides with polycarbonate sheets. These transparent sheets allowed to capture multi-phase development by high-speed camera Photron Fastcam SA-1. Also, to illuminate the chamber space with three 80 and 38 W LED panels. Besides a high-speed camera, the three-way valve and the data acquisition system were triggered concurrently by the Quantum generating unit.

3. Experimental results and discussion

A series of experiments were conducted for the following liquid volume fractions (LVF): 96.4, 83, 73, 62.5, 52, 35.1, and 0%. The initial conditions were the same for all tests with atmospheric temperature in the three sections (19–23°C). While it was 2.6–2.9 in the MPS and 5.3–5.6 MPa in the conical vessel, the chamber pressure was atmospheric (0.1 MPa).

3.1. Features of explosive evaporation from the conical vessel

Fig. 2 shows the variation in pressure sensors records over a 50 ms period of CO_2 depressurization. The LVF for (a) was 0, (b) 62.5, and (c) 96.4%. Correspondingly, the temperature change (d), (e), and (f). The

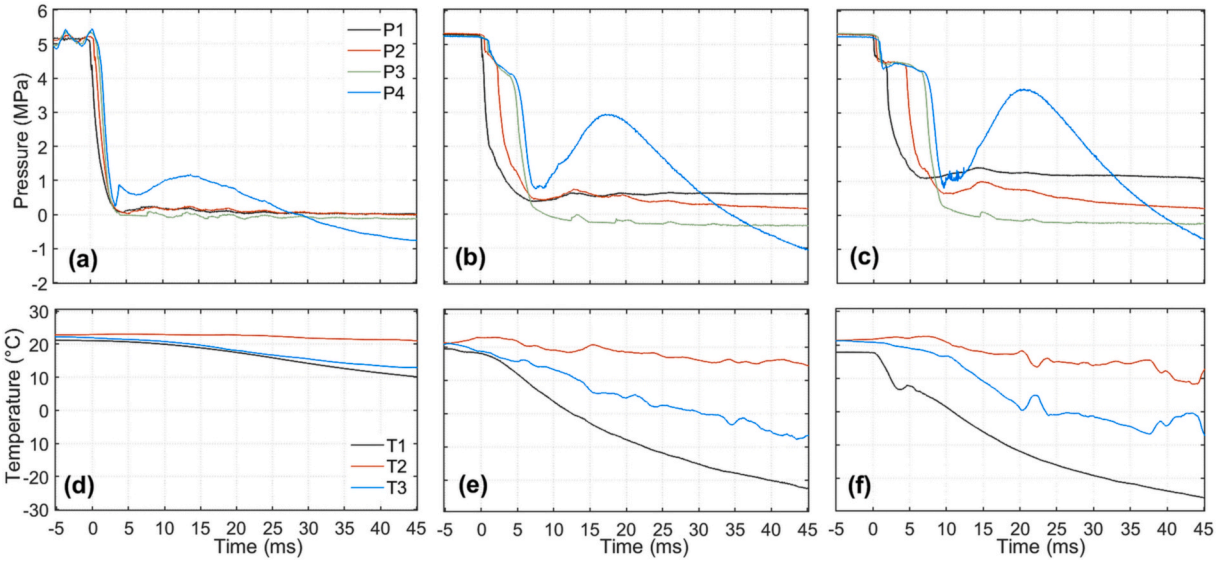

Fig. 2. Graphs from the pressure and temperature sensors' records P1–P4 and T1-T3 (top to bottom) during 50 ms of CO_2 decompression. For LVF 0% (a, d), 62.5% (b, e), and 96.4% (c, f).

pressure sensors (P1–P4) are positioned at 285, 185, 85, and 35 mm from top to bottom, and the temperature sensors (T1-T3) at 285,185 and 35 mm. Time 0 indicates the diaphragm rupture and the first pressure drop.

From the data in Fig. 2, when the HP diaphragm ruptured, the pressure fell sharply to temporary metastable liquid pressure. It is about 4.7 for (b) and 4.5 MPa for (c). Subsequently, it either declined steadily (b) or plateaued (c) until the liquid superheated and entered into the metastable state then started to evaporate. This behaviour was not observed in (a) as the LVF was 0%. The turns of the second rapid pressure drop corresponding to the onset of change in the density. Also, indicate a locus of the propagated front where a significant part of phase transition followed behind it. Similar behaviour has been reported by Chaves [24] and later by Simões-Moreira [25]. The pressure steeply fell until it reached between 0.3 and 1 MPa and then gradually decreased to atmospheric. Tiny fluctuations were observed during the latter pressure decrease on lines P1–P3. However, a characteristic development was observed in the bottom pressure transducer P4 signals. It had different record trails with intense oscillations followed by a considerable increase in pressure. As seen in Fig. 2 (a,b, and c), the pressure curve P4 amplitudes increase with increasing the LVF from (a) to (c). The pressure rise depends on the liquid fraction that these reflected waves pass through. So, the pressure curve peaked at 1.1 for (a), 2.9 for (b), and 3.7 MPa for (c). And at the time about 14, 17.6 and 20.4 ms respectively. Unsurprisingly, the temperature decreases during the evaporation process with increasing LVF. The readings from the top temperature sensor for 0–96.4% LVF show a decrease in about 35 °C after 45 ms (see above Fig. 2 (d,e, and f)). The observed pressure change in the P4 curve could be attributed to the expansion wave reflection on the vessel bottom. Which essentially affected the nearest transducer (P4). The compression is most likely caused by the rapid increase of vapour volume above the pressure transducer site. It might also be the damping effect of heterogeneous nucleation and the consequence of multiple reflections of the rarefaction wave from the vessel's bottom. The latter is explained in the next section.

The rarefaction wave propagated downwards through the vapour phase at the sound speed of the gas. A part of this wave reflected on the vapour/liquid contact surface and directed back into the vapour phase. Subsequently, a slight pressure rise (0.01–0.07 MPa) due to the compression observed on the P1-lines in (b and c) Fig. 2. As the LVF increased in the vessel, the liquid prolonged its state as superheated. Subsequently, the pressure indicated a nearly steady profile. For example, this trend can be seen on P2 lines with plateaus for 96.4% LVF and a slight decline for 62.5% LVF (see Fig. 3 below).

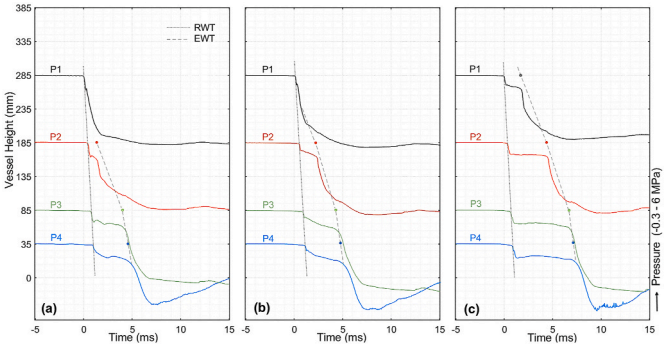

Fig. 3. Pressure transducers readings on vessel height-axis during 20 ms of depressurization of liquid CO_2. For LVF of 35.1% in (a), 62.5% in (b) and 96.4% in (c). The liquid height in the vessel was 134.1, 239.4 and 369.2 mm, correspondingly. The graph also shows the trajectories of rarefaction waves (RWT) and evaporation waves (EWT).

3.2. Dynamic characteristics of the expansion waves

The pressure-time readings were drawn on vessel height versus time scale to measure the characteristic velocities of expansion waves. Wherein the synchronized pressure-time lines begin at the corresponding transducer position and the initial pressure value. Fig. 3 illustrates pressure records on vessel height scale during 25 ms of liquified CO_2 depressurization. For LVF of 35.1, 62.5, and 96.4%.

The curve's points where the first and the second pressure sharply fell represent a trajectory-time for rarefaction wave and evaporation wavefront. The evaporation wave path passes through the time points of pressure change at a stationary height level. As seen in Fig. 3, the evaporation wavefront path is not linear. That is, it propagates with non-constant velocity. As the LVF increases, its propagation starts to delay. As a result, the evaporation wavefront speeds up as it propagated downwards. The rarefaction wave and evaporation wavefront velocities were analyzed graphically based on the time between the turns in pressure sensors readings. Tangent lines were drawn for each pressure reading on the two sides of the curve. Then the tangents' crossing point was connected to the centre point on the line linking the tangency points. This line crossed the curve at a point that allocated the pressure change time.

The results obtained from velocities calculation in the three vessel's height regions are set out in Table 1. The uncertainty in velocities calculation was due to measurement errors of turning points where the pressure fell. The calculation errors were estimated to be between ±0.4 and ± 0.6 m/s for rarefaction waves, ±1.3 and ± 3.5 m/s for evaporation wavefront. The Mjaavatten version of SW-EOS [23] and tabulated data from SW-EOS [20] were used to compute the speed of sound based on the experimental range of saturated CO_2 temperatures 19.5–17.2°C. The average sound speed was 267.2–266.2 m/s. Correspondingly, it was 342.6–370.5 m/s for the liquid phase and 196.6–199.2 m/s for the vapour phase. It is apparent from this table that the evaporation wavefront speeds up as it propagated downwards. The highest speed is in the region between the vessel's height of 85 and 35 mm.

The Pressure-Time-Height graph and velocity calculations were plotted on the height-time diagram to clarify the expansion waves movement and possible reflections interactions. Fig. 4 shows the difference between rarefaction (RW) and evaporation (EW) waves trajectories and their propagation speed. The LVF for (a) is 62.5% and for (b) is 96.4%. In addition, the grey lines show possible reflections after the RW hit the vessel bottom. The liquid height in the vessel substantially influenced those velocities.

After the first pressure drop, the rarefaction wave swiftly passthrough. Depending on the liquid height in the vessel (or LVF), its acceleration intensifies. (see Table 1). That implies it reached the vessel's bottom and reflected faster with increasing LVF. As the LVF increases, a prolonged time is expected for the liquid to stay in the metastable state. That leads to many rarefaction wave reflections between the vessel's bottom and the propagated evaporation wave, as in Fig. 4. It is also seen from the fluctuations just after the rarefaction wave passage, Fig. 2 (b and c). From these fluctuations, some rarefaction wave reflection velocities have been approximated between 192 and 222 m/s.

The fluctuations that emerged from wave reflections in this region were probably comparable to those developed after the evaporation wave has passed. P4 pressure records, Fig. 2 (b and c), required 2.31 ms to drop from 4.01 to 0.83 MPa, and 1.87 ms from 4.08 to 0.89 MPa, for 62.5% and 96.4% LVF, respectively. These numbers explain the disparity in the pressure rise amplitudes after the evaporation wave has passed between 62.5 and 96,4% LVF. The rapid evaporation due to the pressure fall to very low, relative to metastable state one, about 0.9 MPa, indicates a sizeable two-phase volume downstream travelling upwards. Simultaneously, as the pressure P4 run to the trough, a part of an upwards moving two-phase flow changes direction towards the bottom. Subsequently, the pressure increases again and peaks before the two-phase travelling upwards. Then the pressure continues its fall to the

Table 1
Calculated velocities for rarefaction wave and evaporation wavefront in the conical vessel's three regions.

Liquid Height (mm)	Cross-section (mm^2)	LVF (%)	Rarefaction Wave Velocity *RWV*/(m/s)				Evaporation Wave Velocity *EWV*/(m/s)		
			Height region (mm)						
			285–185	185–85	85–35	Average	285–185	185–85	85–35
134.1	277.5	35,1	199.4	291.6	249.1	246.7	–	37.6	88.9
239.4	880.4	62.5	244.3	293.2	245.3	260.9	46.3	47.6	107.1
369.2	2093.9	96,4	300	320	240	286.7	37.8	42.7	111.6

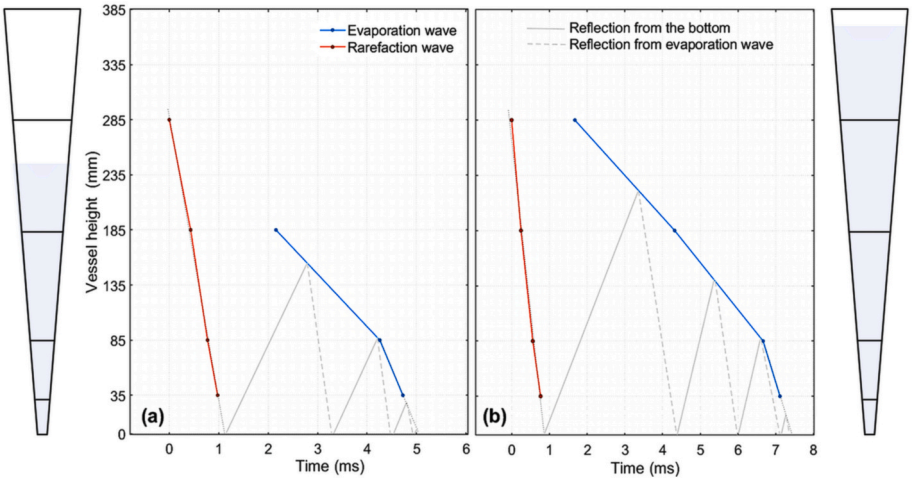

Fig. 4. Height-time graph demonstrating the rarefaction and evaporation wave propagation speed for 62.5 and 96.4% LVF, (a) and (b), respectively. Besides, the potential reflections between the vessel's bottom and the descended evaporation wave. Vessels sketches on the sides show the liquid level. The split lines signify the pressure transducers positions.

atmospheric pressure.

The thermodynamic state after the HP diaphragm rupture is traced by isentropic expansion. From the pre-ruptured saturated liquid to the superheated liquid in the metastable state. The thermodynamic properties in the metastable state were determined by applying the Mjaavatten version SW-EOS [23]. Fig. 5 presents pressure-specific volume *P-v* (a) and pressure-temperature *P-T* (b) phase diagrams. Wherein the former, an isentropic expansion performed by SW-EOS is presented on the P-v plane. In the latter, a possible path through the states is plotted based on experimental data, LVF of 96.4%.

The isentrope from 5.36 to 4.4 MPa is shown as a line connected states 0 to 1, Fig. 4 (a). The density correspondingly decreased to about 7 $kg\cdot m^3$. Besides, the calculated speed of sound at the metastable boundary at point 1 was 341.3 m s. Fig. 5, (b) shows a similar expansion on the possible track line in the P-T graph. On the continuous states' development, point 2 denotes the conditions immediately after the second pressure drop. But not at the vessel's exit. The expansion rate (R_{exp}) was determined from the density decrease during the isentropic expansion and the wave velocity at the metastable limit. The estimated R_{exp} was 2389.1 $kg\cdot m^2\cdot s$.

3.3. Comparison with CO_2 depressurization results from a constant cross-section test device

According to Reinke [26] and Chaves [24], contrary to the current study results, the test device geometry does not influence the

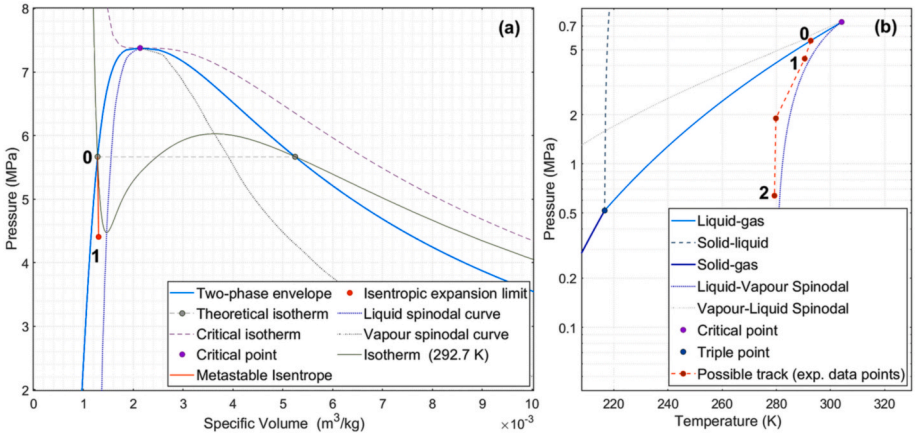

Fig. 5. **(a)** Pressure-specific volume phase diagram shows an isentropic expansion from saturated liquid state 0 to metastable state 1. **(b)** Pressure-temperature phase diagram displaying potential trajectory through the experimental states data P4 in Fig. 2-c.

evaporation wave movement and velocity. However, in the Reinke et al. study [15], the boiling front velocity was observed in different diameter tubes inserted into the test tube. They noticed that the front movement is affected by the tube wall. Subsequently, the velocity increased slightly with the decrease in tubes' diameter. But they mentioned that there was no significant effect of the cross-section area on the front velocity. At this juncture, the above velocity calculations are partly agreed with this observation. However, as stated earlier, the evaporation wave propagation speeded up considerably downwards (see Table 1). The different results from the mentioned studies were probably due to the decompression of other substances than CO_2 (Perfluoro-n-hexane, butane. propane, Refrigerant-134a, and water). It is also possible dissimilar details in the test device geometry.

Comparing the above-calculated velocities and those obtained from CO_2 depressurization in constant cross-section in previous research indicates notable differences in evaporation wave behaviour. In their studies, Hansen [19] and Tosse [27] described an evaporation wave propagated at a nearly constant velocity between 20 and 42 m/s. Whereas in the conical vessel, it travels at a higher speed in varied regions. Particularly in the zone close to the bottom (107,1–111.6 m/s), see Table 1.

3.3.1. Comparison of pressure profiles

The pressure records shown in Fig. 2 (b and c) were compared to those achieved by Hansen [21] To capture detailed differences. CO_2 depressurization was conducted on a rectangular duct with a constant cross-section for 0 and 100% LVF. (the 100% is a possible visual height which corresponds to 68% of the duct's volume). Fig. 6 compares the pressure histories in the rectangular duct (D) and the conical vessel (CV). The corresponding contrasted LVF are both 0% in (a), 100% and 62.4% in (b), and 100% and 96.4% in (c). Pressure sensors were positioned on the upper part of the rectangular duct at 31, 81.8, and 132.8 mm from the top. In comparison, they sited at 98, 198, and 298 mm on the conical vessel from the top. The conical vessel has an extra 59 mm in inner height compared to the rectangular duct.

The pressure drop required more time in the rectangular duct during the evaporation process than the conical vessel. As seen in Fig. 6 (b, c), the additional time was about 21 ms to approach atmospheric pressure. It signifies that the two-phase flow downstream in the rectangular duct was not moving spontaneously. Instead, it probably choked or was disturbed due to a small cross-section in the exit for expanded two-phase flow. On the other hand, the two-phase flow in the conical vessel was propagating in a gradually increasing cross-section towards the exit.

The data in Fig. 6 shows considerable fluctuations in the rectangular duct's pressure lines. In contrast, no such pattern is related to the pressure records from the conical vessel upper part. There are two likely explanations for the former behaviour. First, the rapid expansion of vapour/liquid phases develops a sizable two-phase flow, which is temporarily trapped before its exit from the duct. Besides, the bubbles' size growth caused by heterogeneous nucleation represses the evaporation process continuation. With the help of high-speed video recordings, Hansen [24] observed heterogeneous wall nucleation in front of the evaporation wave. He mentioned that it led to the reduction in the degree of superheat in the rectangular duct set-up. After the first drop in pressure and initiation of the rarefaction wave, the liquid in the conical vessel had remained longer in the metastable state than in the duct before the evaporation wave started its propagation. This difference is between the first and the start of the second pressure drop (see Fig. 8 below).

3.3.2. Clarifications about initial conditions

The pre-rupture pressure in the conical vessel experiments varied from those conducted in the rectangular duct. However, the conical vessel is a part of an arrangement that has a double-diaphragm rupturing mechanism. The medium-pressure diaphragm ruptured first due to increased pressure in the medium section. As a result, the high-pressure (HP) diaphragm bulged. Subsequently, the pressure inside the conical vessel became unsteady and reduced. Then it stabilized again before the

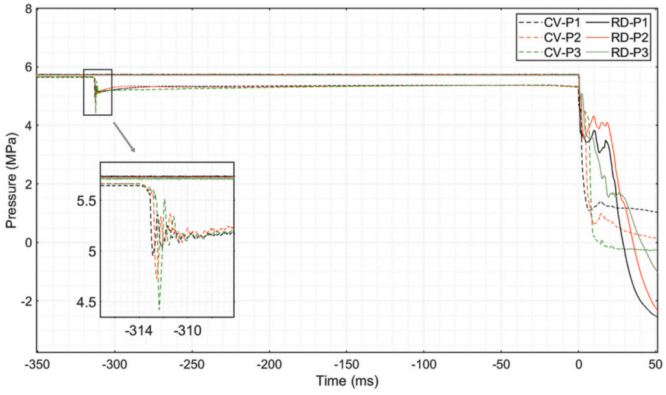

Fig. 7. Pressure signals recorded in the experiments shown in Fig. 6 (c), including 350 ms before the HP-diaphragm ruptured in the rectangular duct and conical vessel. The close-up section shows the pressure response to the MP-diaphragm rupturing in the conical rig.

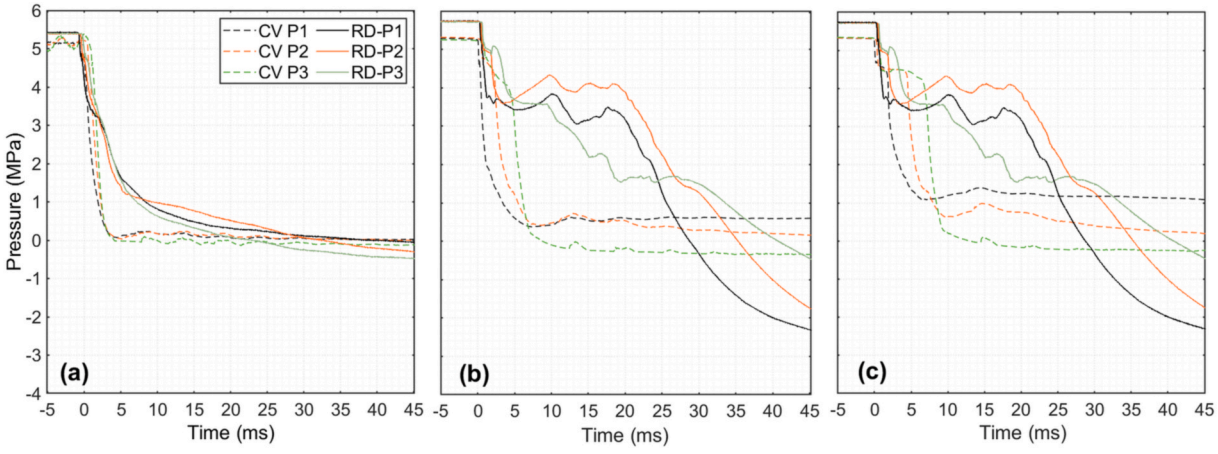

Fig. 6. Comparison of Pressure sensors readings over 50 ms of CO2 depressurization from the rectangular duct and the conical vessel. (a) for 0%, (b) for 100 and 62, 5%, and (c) for 100 and 96.4% LVF.

HP-diaphragm has ruptured. The difference in pre-ruptured pressure between the two devices is about 0.36 MPa. Pressure records from the experiments displayed above in Fig. 6 (c) are compressed to cover 350 ms before the HP-diaphragm ruptures. It is illustrated in Fig. 7 for both rectangular duct and conical vessel. The graph contains an enlarged segment showing the MP-diaphragm rupturing at about 313 ms before the HP-diaphragm ruptured. The initial temperature was 292.7 K. After the MP-diaphragm rupturing in the conical vessel, the observed temperature change was minimal, about 3 K.

3.3.3. Comparison of expansion flow characteristics

The evaporation wave speed mostly depends on the degree of superheating (DOS) [14]. Which is defined as the maximum expansion in the metastable region and expressed by Simões-Moreira [25] as $(P_s - P_m)/P_s$. Where P_s is saturated pre-rupture pressure, and P_m is metastable limit pressure after the isentropic expansion (at state 1 in Fig. 5 (a)).

Fig. 8 represents enlarged segments comparing the pressure profiles shown in Fig. 6 during 10 ms of liquified CO_2 decompression in the conical vessel and the rectangular duct. The LVFs were 0% in (a), 62.5 and 100% in (b), 96.4 and 100% in (c), correspondingly.

For the duct's experiments with 100% LVF, the pressures dropped during isentropic expansion from 5.84 to 5.50 MPa. The corresponding DOS was about 0.14. On the other hand, during isentropic expansion in the conical vessel experiments (62.5 and 96.4% LVF), the pressures fell from 5.36 to 4.40 MPa and 5.28 to 4.05 MPa. The resultant DOS were 0.18 and 0.23, respectively. Other experimental results done by Hansen [28] on the rectangular duct demonstrated much lower DOS (0.11). It is noticeable from these numbers that the DOS was higher in the experiments conducted in the conical vessel than those in the duct. Moreover, this also explains why the evaporation wave velocities were higher in the conical vessel than in the duct. Table 2 below compares the pre-ruptured saturated state and calculated properties for supersaturated liquid after isentropic expansion in the metastable region.

This table is quite revealing in several ways. First, the differences in upstream properties between the conical vessel and the rectangular duct were caused by the variation in DOS at the metastable state. There is a difference in the DOS of about 0.09 between the vessel and duct. This variation could have led to the mentioned disparity of the other properties (density and enthalpy). Second, the difference between calculated evaporation wave velocities grew as the conical vessel's cross-section decreasing. The difference was 73.5 m/s in the region close to the bottom and 0.3 m/s at the upper zone. The velocity is nearly constant for the rectangular duct. Third, since the evaporation wave velocity increased downward and the cross-section upward in the conical vessel, further discrepancies are expected to detect in downstream properties.

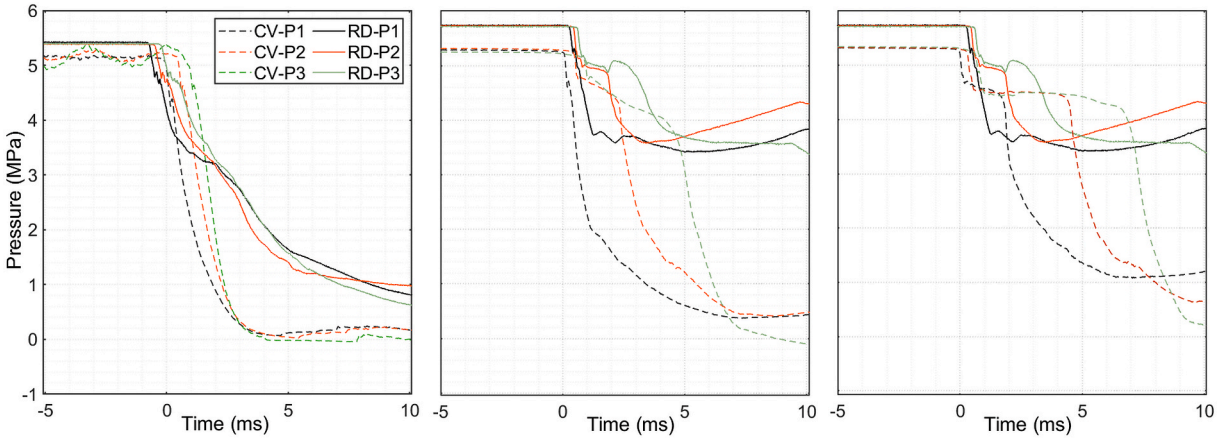

Fig. 8. Comparison of Pressure sensors readings over 10 ms of CO2 depressurization from the rectangular duct and the conical vessel. (a) for 0%, (b) for 100 and 62, 5%, and (c) for 100 and 96.4% LVF.

Table 2
Pre-ruptured at the saturated state and calculated metastable upstream properties. The experiments were performed in the rectangular duct (100% LVF) and conical vessel (96.4% LVF).

Property		Rectangular Duct	Conical Vessel
Saturated State	Pre-rupture pressure P_0/ (Mpa)	5.8	5.4
	Temperature T/ (K)	294	290.3
	Density ρ/ (kg/m^3)	764.4	801.3
Upstream Metastable State	Metastable limit pressure P_1/ (Mpa)	5.0	4.4
	Density ρ/ (kg/m^3)	756.7	794.3
	Maximum EW velocity v_{max}/ (m/s)	38.1	111.6
	Minimum EW velocity v_{min}/ (m/s)	38.1	37.8
	Enthalpy h_1/ (kJ/kg)	257.6	245.4
	DOS	0.14	0.23

4. Conclusion

Laboratory-scale experiments were conducted in a double-diaphragm installation that comprises a divergent cross-section vessel as a high-pressure section. The rarefaction and evaporation wavefront velocities were analyzed in three vessel's regions lengthwise based on the pressure histories. Results indicated that the evaporation wavefront velocity increased with decreased cross-section area and increasing liquid volume fraction (LVF). The calculated highest and lowest velocities were 111.6 and 37.8 m/s in the region close to the vessel's bottom and upper region, respectively, for 96.4% LVF. Besides, the thermodynamic properties of superheated CO_2 in the metastable state were determined utilizing the Span-Wagner equation of state. The obtained results were compared with previous experimental results from CO_2 depressurization in a vertical rectangular duct.

There are notable differences in expansion wave features in the two cases. First, the duct's exit cross-section did not allow instantaneous passage of rapidly expanded two-phase flow. In comparison, it moved in an increased cross-section towards the exit in the conical vessel. Second, the evaporation wave velocity was steady in the constant cross-section devices. In contrast, it increased in the conical vessel as the cross-section area shrank. Third, significant disparities in the upstream properties were caused by corresponded variation in the degree of superheating during the isentropic expansion in the metastable region. These differences are anticipated to influence downstream properties significantly.

Funding

This research did not receive any specific grant from funding agencies in the public, commercial, or not-for-profit sectors.

Credit Author Statement

Osama M.Ibrahim: Conceptualization, Methodology, Investigation, Writing – original draft, Visualization, Formal analysis. **Per Morten Hansen:** Methodology, Conceptualization, Resources, Writing- Reviewing and editing, Supervision. **Dag Bjerketvedt:** Conceptualization, Formal analysis, Writing- Reviewing and editing, Supervision. **Knut Vågsæther:** Conceptualization, Methodology, Validation, Resources, Writing- Reviewing and editing, Supervision, Project administration.

Declaration of competing interest

The authors declare that they have no known competing financial interests or personal relationships that could have appeared to influence the work reported in this paper.

References

[1] I.E. Agency, 20 Years of Carbon Capture and Storage, 2016.
[2] G. Cheng, M. Zhang, Y. Cao, Y. Lu, Y. Feng, S. Zhao, Preparation and evaluation of lignite flotation collector derived from waste hot-pot oil, Fuel 267 (2020) 117–138.
[3] G. Cheng, Z. Li, Y. Cao, Z. Jiang, Research progress in lignite flotation intensification, International Journal of Coal Preparation and Utilization 40 (1) (2020) 59–76.
[4] A.C. Van den Berg, M.M. Van der Voort, J. Weerheijm, N.H.A. Versloot, BLEVE blast by expansion-controlled evaporation, Process Saf. Prog. 25 (1) (2006) 44–51.
[5] CCPS (Center for Chemical Process Safety), Guidelines for Vapor Cloud Explosion, Pressure Vessel Burst, BLEVE, and Flash Fire Hazards, second ed., Process Safety Progress, Wiley, New York, 2010, pp. 311–336.
[6] R.C. Reid, Superheated liquids, Am. Sci. 64 (2) (1976) 146–156.
[7] R.C. Reid, Possible mechanism for pressurized-liquid tank explosions or BLEVE's, Science 203 (4386) (1979) 1263–1265.
[8] M.M. van der Voort, A.C. van den Berg, D.J.E.M. Roekaerts, M. Xie, P.C.J. de Bruijn, Blast from explosive evaporation of carbon dioxide: experiment, modeling and physics, Shock Waves 22 (2) (2012) 129–140.
[9] Y. Zhang, J. Schork, K. Ludwig, Revisiting the conditions for a CO2 tank explosion, in: Proceedings of the Ninth Global Congress on Process Safety, AIChE, San Antonio, Texas, 2013.
[10] D. Bjerketvedt, K. Egeberg, W. Ke, A. Gaathaug, K. Vaagsaether, S.H. Nilsen, Boiling liquid expanding vapour explosion in CO_2 small scale experiments, Energy Procedi 4 (2011) 2285–2292.
[11] T. Abbasi, S.A. Abbasi, Accidental risk of superheated liquids and a framework for predicting the superheat limit, J. Loss Prev. Process. Ind. 20 (2007) 165–181.
[12] J.R. Simões Moreira, J.E. Shepherd, Evaporation waves in superheated dodecane, J. Fluid Mech. 382 (1999) 63–86.
[13] CCPS (Center for Chemical Process Safety), Guidelines for Evaluating the Characteristics of Vapor Cloud Explosions, Flash Fires, and BLEVEs, Wiley, New York, 1994, pp. 60–160.
[14] L.G. Hill, An Experimental Study of Evaporation Waves in a Superheated Liquid, PhD Thesis, California Institute of Technology, USA, Pasadena, California, 1991.
[15] P. Reinke, G. Yadigaroglu, Explosive vaporization of superheated liquids by boiling fronts, Int. J. Multiphas. Flow 27 (2001) 1487–1516.
[16] S. Gourari, F. Mebarek-Oudina, O. Makinde, M. Rabhi, Numerical investigation of gas-liquid two-phase flows in a cylindrical channel, Defect Diffusion Forum 409 (2021) 39–48.
[17] A.M. Nagib Elmekawy, M.E.H.H. Ali, Computational modeling of non-equilibrium condensing steam flows in low-pressure steam turbines, Result. Eng. 5 (2020) 100065.
[18] G. Pinhasi, A. Ullmann, A. Dayan, Numerical model for boiling liquid-vapour explosion (BLEVE), Int. J. Heat Mass Tran. 50 (2007) 4780–4795.
[19] P.M. Hansen, A.V. Gaathaug, D. Bjerketvedt, K. Vaagsaether, Rapid depressurization and phase transition of CO_2 in vertical ducts – small-scale experiments and Rankine-Hugoniot analyses, J. Hazard Mater. 365 (2019) 16–25.
[20] R. Span, W. Wagner, A new equation of state for carbon dioxide covering the fluid region from the triple-point temperature to 1100 K at pressures up to 800 MPa, J. Phys. Chem. Ref. Data 25 (6) (1996) 1509–1596.
[21] K.E.T. Giljarhus, S.T. Munkejord, G. Skaugen, Solution of the Span–Wagner equation of state using a density–energy state function for fluid-dynamic simulation of carbon dioxide, Ind. Eng. Chem. Res. 51 (2012) 1006–1014.
[22] P. Hansen, Experimental and Theoretical Studies of Rapid Phase Transitions in Carbon Dioxide, PhD Thesis, Process, Energy and Automation Engineering, University of South-Eastern Norway, Porsgrunn, Norway, 2018.
[23] A. Mjaavatten, Thermodynamic Models and Tools for H_2O, H_2, CO_2 and Air, GitHub, 2020. https://github.com/are-mj/thermodynamics/releases/tag/v2.1.
[24] H. Chaves, Changes of Phase and Waves on Depressurization of Liquids with High Specific Heat, PhD Thesis, Max-Planck-Institut für Strömungsforschung, Göttingen, Germany, 1984.
[25] J.R. Simões-Moreira, J.E. Shepherd, Adiabatic Evaporation Waves, PhD Thesis, Department of Mechanical Engineering, Rensselaer Polytechnic Institute, Troy, N. Y, 1994.
[26] P. Reinke, Surface Boiling of Superheated Liquid, PhD Thesis, Paul Scherrer Inst. (PSI), Villigen, Switzerland, 1997.
[27] S. Tosse, K. Vaagsaether, D. Bjerketvedt, An experimental investigation of rapid boiling of CO2, Shock Waves 25 (3) (2015) 277–282, 2015.
[28] P.M. Hansen, A.V. Gaathaug, D. Bjerketvedt, K. Vaagsaether, Blast from pressurized carbon dioxide released into a vented atmospheric chamber, Shock Waves 28 (5) (2018) 1053–1064.